Phononic drumhead surface state in the distorted kagome compound RhPb

Andrzej Ptok [1,*] William R. Meier [2,†] Aksel Kobiałka [3] Surajit Basak [1] Małgorzata Sternik [1]
Jan Łażewski [1] Paweł T. Jochym [1] Michael A. McGuire [2] Brian C. Sales [2] Hu Miao [2]
Przemysław Piekarz [1] and Andrzej M. Oleś [4,5,‡]

[1]*Institute of Nuclear Physics, Polish Academy of Sciences, W. E. Radzikowskiego 152, PL-31342 Kraków, Poland*
[2]*Material Science & Technology Division, Oak Ridge National Laboratory, Oak Ridge, Tennessee 37831, USA*
[3]*Department of Physics, University of Basel, Klingelbergstrasse 82, CH-4056 Basel, Switzerland*
[4]*Max Planck Institute for Solid State Research, Heisenbergstrasse 1, D-70569 Stuttgart, Germany*
[5]*Institute of Theoretical Physics, Jagiellonian University, Prof. Stanisława Łojasiewicza 11, PL-30348 Kraków, Poland*

RhPb was initially recognized as one of CoSn-like compounds with $P6/mmm$ symmetry, containing an ideal kagome lattice of d-block atoms. However, theoretical calculations predict the realization of the phonon soft mode, which leads to the kagome lattice distortion and stabilization of the structure with $P\bar{6}2m$ symmetry [A. Ptok *et al.*, Phys. Rev. B **104**, 054305 (2021)]. Here, we present the single crystal x-ray diffraction results supporting this prediction. Furthermore, we discuss the main dynamical properties of RhPb with $P\bar{6}2m$ symmetry, i.e. phonon dispersions and surface Green's functions using the modern theoretical methods based on density functional theory. The bulk phononic dispersion curves contain several flattened bands, Dirac nodal lines, and triple degenerate Dirac points. As a consequence, the phononic drumhead surface state is realized for the (100) surface, terminated by the zigzaglike edge of Pb honeycomb sublattice.

I. INTRODUCTION

Discovery of the topological insulators with conducting surface states in the form of the Dirac cone [1–4] opened a period of intensive studies in the subject of fermionic topological systems [5–7]. However, a realization of the nontrivial topological states is not limited only to fermionic systems, but can be also expected in bosonic ones as well [8–12]. We can find several examples of the occurrence of phonon Dirac/Weyl points [13–27], nodal lines [28–33], nodal rings [33–38], and nodal nets [39–42]. Topological properties are also manifested by the emergence of phonon surface states [15–19,32,35,36,43–49] or phonon Hall effect [50–56]. As a result, existence of the topological phonons with nonzero Berry curvature [57] can give rise to the development of nanodevices based on the heat transfer manipulation, i.e., in phononics [58].

In the context of the topological properties, the kagome-supported systems have been of great interest recently. The basic property of the system with the kagome lattice is the formation of flat electronic bands [59–61]. One such example of the kagome systems are CoSn-like compounds, which combine kagome and honeycomb layers [62–65]. The electronic band structure exhibits a flat band and Dirac fermions [62–70]. Some CoSn-like compounds exhibit frustrated magnetism with an important role for itinerant electrons [71], like magnetically ordered FeGe [72], or FeSn [62,70,73,74]. However, most commonly, these compounds are paramagnets, such as CoSn [73].

Motivation: Typically, the kagome net CoSn-like compounds crystallize with the $P6/mmm$ symmetry [62,63]. In such a structure, the d-block element (e.g., Fe, Co, Ni, Rh, or Pt) forms an ideal kagome sublattice, while the p-block element (e.g., Ge, In, Sn, Tl, or Pb) has two nonequivalent positions: one of the p-block elements is located in the plane of the kagome sublattice when the second's position forms honeycomb sublattice intercalated between two kagome-sublattice planes. RhPb satisfies the mentioned conditions, and therefore it should behave as an ideal kagome metal [63]. However, theoretical investigations of the lattice dynamics of RhPb show that this compound should be unstable with the $P6/mmm$ symmetry [75]. Stabilization of RhPb can be achieved by distorting the kagome lattice, resulting in the $P\bar{6}2m$ symmetry (see Fig. 1). In this paper, we present experimental evidence for the distorted kagome structure in the RhPb system. Furthermore, we investigate the dynamic properties of RhPb with a distorted kagome lattice. We show that this compound is an excellent candidate for the study of the phonon drumhead surface state.

The paper is organized as follows. First, we discuss the results indicating formation of the distorted kagome lattice in RhPb with the $P\bar{6}2m$ symmetry (Sec. II). Next, we present
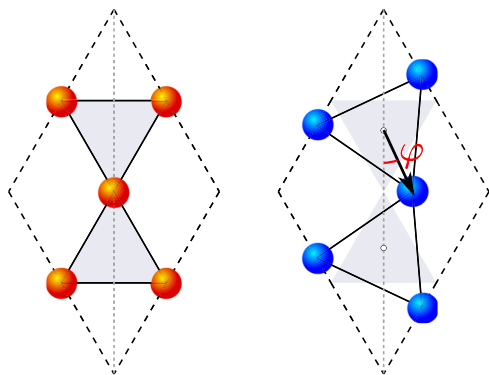

FIG. 1. Schematic representation of the ideal (left panel) and distorted (right panel) kagome lattices, realized in the system with symmetries $P6/mmm$ and $P\bar{6}2m$, respectively. In the ideal kagome lattice, the system is centrosymmetric. The rotation of perfectly ordered triangles by angle φ transforms the system into the noncentrosymmetric structure.

the theoretical study of the dynamical properties of this compound (Sec. III). Finally, we summarize the paper with the main conclusions in Sec. IV.

II. CRYSTAL STRUCTURE

Crystals of RhPb were grown from a high-temperature Pb-rich melt [63]. A 1:3 atomic ratio of rhodium sponge (Alfa Aesar 99.95%) and lead slugs (Alfa Aesar Puratronic 99.999%) were loaded into one side of a 2 mL alumina Canfield crucible set [76] and then sealed in a fused silica ampule under vacuum with a hydrogen-oxygen torch. The ampule was placed in a box furnace and heated to 1000 °C or 1100 °C over 6 h. This temperature was held for 2 h to dissolve the rhodium in lead and homogenize the fluid. The furnace was quickly cooled to 900 °C over 3.5 h and held for 0.5 h before cooling to 750 °C over 320 h (−0.47 °C/h) to slowly precipitate the crystal. The hot ampule was removed from the furnace and inverted into a centrifuge to fling the remaining liquid of the crystals. In the batch used for single crystal diffraction, 5.4 g of reactants yielded a single 4×7 mm crystal weighing about 1.2 g. It had a slightly skeletal hexagonal-prismatic shape with a shiny metallic cluster [see Fig. 2(a)]. Other batches of crystals yielded faceted euhedral blocky hexagonal prisms. Crystals of RhPb are brittle with a conchoidal fracture and have weak (001)-cleavage. Broken surfaces sometimes reveal
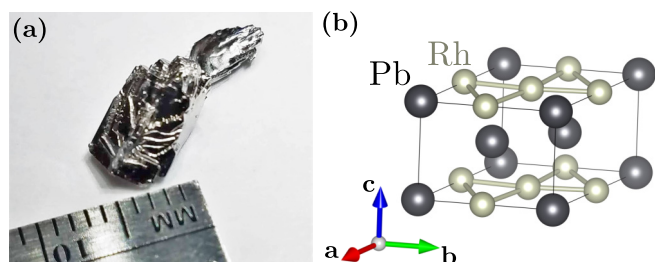

FIG. 2. Single crystal of RhPb grown from lead melt (a), and crystal structure of RhPb with $P\bar{6}2m$ symmetry (b).

TABLE I. An important characteristic of refined structures of RhPb at 293 K from single crystal x-ray diffraction. Note the significant improvement of fit quality in the $P\bar{6}2m$ refinement.

Space group	$P6/mmm$	$P\bar{6}2m$
x_{Rh}	1/2	0.4775(2)
Twin fraction	N/A	0.568(25)
Triangle rotation, φ in Fig. 1	0°	4.45(3)°
R(obs) (%)	6.01	2.83
Goodness of fit obs	4.91	1.65

inclusions of bluish metallic Pb metal that contrast with the silver metallic RhPb surfaces.

To determine the crystal structure of RhPb, fragments of the 1.2 g crystal were selected for single crystal x-ray diffraction (XRD). The crystal, approximately $60 \times 40 \times 10$ μm^3, was mounted on the end of a Kapton loop with Locktite glue for data collection at room temperature using a Bruker D8 Quest diffractometer (0.71073 Å Mo K$_\alpha$ radiation). Data were collected, reduced, and analyzed using APEX3 software, including a semiempirical absorption correction based on equivalent reflections. Structure refinement was performed using JANA 2020 [77] for both $P6/mmm$ (space group No. 191) and $P\bar{6}2m$ (space group No. 189) symmetries.

The first-principles density functional theory (DFT) calculations were performed using the projector augmented-wave (PAW) potentials [78] implemented in the Vienna *ab initio* simulation package (VASP) code [79–81]. Calculations were made within the generalized gradient approximation (GGA) in the Perdew, Burke, and Ernzerhof (PBE) parametrization [82]. The energy cutoff for the plane-wave expansion was set to 350 eV. Optimizations of structural parameters (lattice constants and atomic positions) were performed in the primitive unit cell using the $10 \times 10 \times 6$ **k**-point grid in the Monkhorst-Pack scheme [83]. As a break condition of the optimization loop, we took the energy difference of 10^{-6} eV and 10^{-8} eV for ionic and electronic degrees of freedom, respectively.

Structure: Initially, the RhPb structure was assumed to possess the $P6/mmm$ symmetry [63]. However, theoretical analysis of the RhPb dynamical properties shows that such a system is unstable [75]. Our single crystal refinement does indeed reveal that RhPb adopts the distorted $P\bar{6}2m$ structure based on a distinctly better fit quality over the $P6/mmm$ solution (Table I). DFT calculations estimate very subtle differences in the lattice parameters for both structures (Table II), but more stable phonons in the $P\bar{6}2m$ structure (detailed discussion in Sec. III A).

In the case of the $P6/mmm$ symmetry, the Rh atoms are located in the Wyckoff position $3f$ (1/2, 1/2, 0), while the Pb atoms in two nonequivalent Wyckoff positions $2d$

TABLE II. Comparison of the experimental and theoretical (DFT) lattice constants for RhPb with different symmetries.

	a (Å)	c (Å)
Exp. 293(2) K	5.6794(4)	4.4311(3)
Exp. 15 K (Ref. [63])	5.66601(2)	4.41267(1)
DFT $P6/mmm$	5.740	4.487
DFT $P\bar{6}2m$	5.762	4.466

(1/3, 2/3, 1/2) and 1a (0,0,0). In the case of the $P\bar{6}2m$ symmetry [see Fig. 2(b)], the 3f position of the Rh atom is calculated to lie at (0.467,0.467,0). Experimentally, the position of the Rh atom was estimated as (0.4775(2),0.4775(2),0). The distortion present in the system corresponds to the rotation of the triangles that form an ideal kagome lattice (see Fig. 1) with angle $\varphi = 6.5°$ determined by DFT, while the experimentally obtained value is 4.46°. The rotation of the kagome triangles in RhPb reflects the modified kagome pattern seen in the ZrNiAl-type materials [84–92]. The $P\bar{6}2m$ space group does not alter the translational symmetry for the lattice and therefore can only be distinguished from $P6/mmm$ by fitting the diffracted intensities. The smaller R and goodness of fit values reported in Table I demonstrate that the lower symmetry structure better models the experimentally observed intensities. More crystallographic data (e.g., CIF files as well as XRD refinements) can be found in the Supplemental Material (SM) [93].

Regardless of the symmetry, RhPb exhibits a metallic band structure (see Fig. S2 in the SM [93]). The electronic band structure obtained for both symmetries is very similar, and in correspondence to other CoSn-like compounds, it contains several flattened bands (detailed discussion can be found in Sec. S2 in the SM [93]).

III. DYNAMICAL PROPERTIES

The dynamical properties were calculated using the direct Parlinski-Li-Kawazoe method [94], implemented in the PHONOPY package [95]. Within this method, the interatomic force constants (IFC) are calculated from the Hellmann-Feynman (HF) forces acting on the atoms after displacements of individual atoms inside the supercell. We performed these calculations using the $2 \times 2 \times 2$ supercell with 48 atoms, and the reduced $\boldsymbol{k}$-point grid $3 \times 3 \times 3$. Next, the IFC were used to study the surface states, by calculations of the surface Green's function for the semiinfinite system [96], using WANNIERTOOLS [97]. Additionally, we also calculate the phonon dispersion curves for a finite temperature. In this case, the calculations were performed for the thermal distribution of multidisplacement of atoms [98], generated within the HECSS procedure [99]. The total energy and HF forces acting on all atoms are calculated with VASP for 100 different configurations of atomic displacements in the supercell. In dynamical properties calculations, we include second- and third-order phonon contributions, which correspond to the harmonic and cubic IFC, respectively.

A. Phonon dispersion curves

The phonon dispersion relations and the phonon density of states (DOS) for RhPb with both symmetries are presented in Fig. 3. In the case of the $P6/mmm$ symmetry, there exists the imaginary soft mode (presented as negative frequencies) [see Fig. 3(a)]. This soft mode, with the frequency of −2.59 THz at the Γ point, is characterized by the B_{1u} symmetry. Atomic displacements induced by this mode lead to the rotation of the triangles forming the ideal kagome lattice [75] (see Fig. 1). As a consequence, the $P\bar{6}2m$ symmetry is stabilized—after the transformation, the phonon dispersion does not exhibit any

imaginary modes, so all frequencies are real [Fig. 3(c)]. The analysis of the zone-center mode frequencies and symmetries shows that in the distorted structure, the mode corresponding to the soft mode has a frequency of 3.2 THz and an A-like symmetry.

Soft modes observed in the $P6/mmm$ symmetry are associated only with the Rh atoms' vibration, which is reflected in the phonon density of states. In practice, all spectral weights at DOS related to the soft mode [negative frequencies in Fig. 3(b)] correspond to the Rh atoms contribution. For negative frequencies, the contribution of Pb atoms is negligible. Indeed, stabilization of RhPb with the $P\bar{6}2m$ symmetry mainly modified the Rh contribution [cf. Figs. 3(b) and 3(d)]. As expected, independently of the system symmetry, the vibrations of the heavy Pb atoms are located mostly in the lower frequency range. The vibrations of lighter Rh atoms exist in the higher frequency range.

Here, we should point out that the spontaneous kagome rotation can also be achieved in other compounds, like $MgCo_6Ge_6$ [100], at $T = 100$ K. Nevertheless, in the case of RhPb, the theoretical investigation of temperature-dependent phonon dispersion for $P6/mmm$ always shows soft mode at the Γ point (even up to 1500 K). From this, we can conclude that the RhPb compound crystallizes only with the $P\bar{6}2m$ symmetry, while the structure with the $P6/mmm$ symmetry is unstable even at high temperatures.

Symmetry realized by RhPb has an impact on the irreducible representation of phonons at the Γ point. Indeed, the exact analysis presented in Sec. S3 in the SM [93] clearly shows differences between these two phases. In fact, due to the different number of active modes in both symmetries, e.g., visible in the Raman spectroscopy, we can gain additional evidence for the formation of the $P\bar{6}2m$ crystal symmetry.

B. Flat phonon bands

Typically, the kagome lattice allows the creation of flat bands—this property is observed in the electronic band structure of CoSn-like compounds [63–66] as well as in their phonon dispersion curves. For both symmetries, there are several flat bands with a weak dispersion along the Γ-K-M-Γ and A-H-L-A paths [e.g., the branch marked in yellow in Figs. 3(a) and 3(c)]. A previous study on the similar CoSn system, suggests that the flat bands are related to the collective vibrations of d-block atoms (i.e., Co) [101]. However, as we have shown for CoSn-like compounds in Ref. [75], phonon bands order results rather from the mass sequence, and the flat bands correspond to the vibrations of the heaviest (p-block) atoms. Also, analysis of the polarization vectors of RhPb phonons, presented here, clearly shows that dispersionless modes are related to the vibrations of Pb atoms [marked with blue arrows in Figs. 3(b) and 3(d)]. Moreover, the flat low-frequency mode corresponds to the vibration of the Pb atom in the Rh kagome net plane (see also partial DOS presented in Fig. S6 in the SM [93]). The separation of Pb phonon modes can be understood by taking into account the significant Pb:Rh mass ratio (207.2:102.9), which is responsible for the relatively weak coupling of Pb vibrations with those of neighboring Rh atoms and justifies the existence of separated and mostly dispersionless mode. Furthermore, in the frequency range of
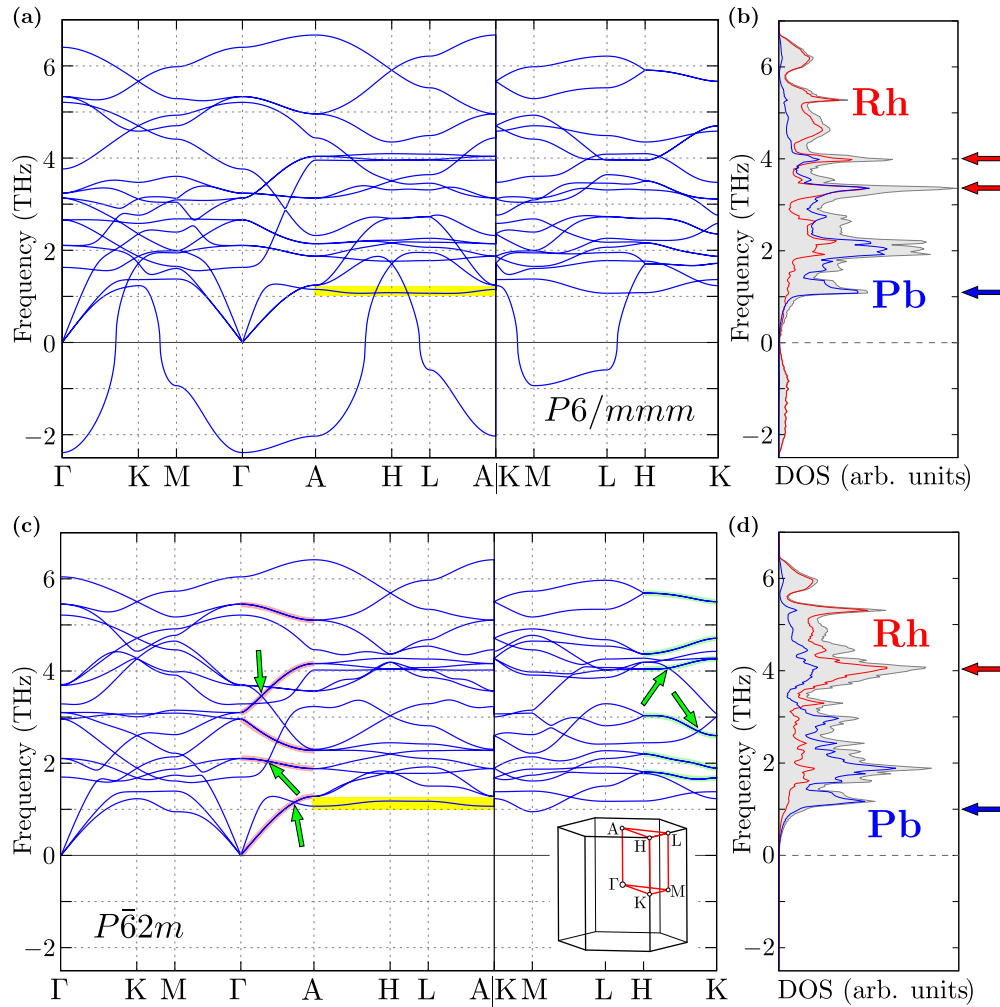
FIG. 3. Phonon dispersion relations (left column) and phonon density of states (right column) for RhPb with $P6/mmm$ (top row) and $P\bar{6}2m$ (bottom row) symmetry. The branches marked with solid light red or light green lines corresponding to the doubly degenerate band along the Γ-A and K-H directions, respectively. Similarly, the green arrows indicate triple degenerate Dirac points resulting from the intersection of the doubly degenerate band with the nondegenerate band. Color lines in the right panels are related to the total DOS (gray) or partial DOS (red and blue for lighter Rh and heavier Pb atoms, respectively). The inset in panel (c) represents the Brillouin zone and its high symmetry points.

flat bands, the chiral phonons (i.e., circulations of the atoms around the equilibrium position) were predicted within the Pb honeycomb sublattice [75].

The occurrence of the mentioned flat bands is reflected in phonon DOS, by the relatively sharp peaks [marked with red arrows in Figs. 3(b) and 3(d)]. Moreover, the phonon DOS describes the frequency distribution of normal modes inside the whole Brillouin zone, in contrast to the phonon dispersion curves which only represent the modes along high symmetry directions. Therefore, the truly flat bands (separated from others' contributions) are represented in DOS for $P6/mmm$ symmetry by very sharp peaks [see Fig. 3(b)]. In the case of $P\bar{6}2m$ symmetry, however, a stronger k dependence of phonon dispersion relations should be noticed, resulting in much broader peaks of phonon DOS [see Fig. 3(d)]. It means, that the phonon bands for the $P\bar{6}2m$ symmetry are more dispersive than in the case of the $P6/mmm$ symmetry.

C. Bands degeneracy and Dirac points/lines

The presence of three and sixfolded rotational symmetry results in preserving band degeneracy of the Γ point also along so-called high-symmetry directions. Indeed, the degeneracy preservation is well visible along the Γ-A path (i.e., for the z direction, perpendicular to the honeycomb and kagome layers) [branches marked with the red solid line in Fig. 3(c)]. Additionally, the hexagonal symmetry affects the band structure along the K-H path, where some bands are double degenerate and form the Dirac nodal lines. Irreducible representations at the K (H) point allow for the realization of double degenerate points. However, the symmetry of this state is preserved for any point P with coordinates $(1/3,1/3,u)$ within the double degenerate state. Finally, the Dirac point at the K (H) point [visible, e.g., in the form of characteristic band crossing around 5.6 THz for both symmetries in Figs. 3(a) and 3(c)], exists along the whole K-H path, forming the Dirac nodal line.
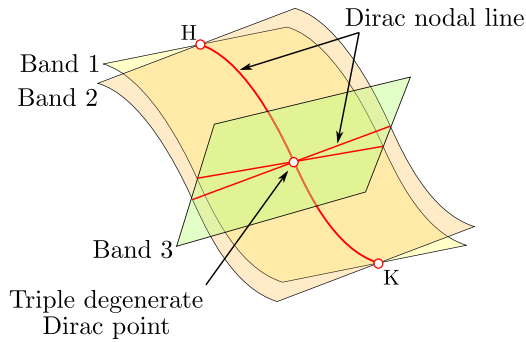
FIG. 4. Schematic representation of triple degenerate Dirac point forming along the K-H path.

The intersections of doubly degenerate and non-degenerate bands occurring along the Γ-A and K-H directions [pointed out by green arrows in Fig. 3(c)] determine Dirac points with a triple degeneracy. Figure 4 schematically illustrates how the Dirac nodal line and triply degenerate Dirac point are defined. Two bands (band 1 and 2) intersecting along the K-H path form a nodal line, and another band (band 3) crossing this line marks a triply degenerate point. Two additional Dirac nodal lines are created where band 3 intersects bands 1 and 2. Here we would like to stress that the realization of (bulk) Dirac point and nodal lines strongly affects the surface states character. In the next paragraph, we will focus on this aspect.

D. Phonon surface states

Some hexagonal lattices, like honeycomb [102–104] and kagome [105,106] nets, can form the electronic surface states at the zigzaglike edge of the lattice. This is also true in the case of the bosonic systems [43,107–110]. Indeed, the phonon zigzag edge modes could be realized in RhPb at the (100) surface [Fig. 5(a)]. Similar behavior was also earlier reported for NbReSi, which possesses the same symmetry [111].

The calculated phonon surface states of RhPb for the (100) surface are presented in Fig. 5. In our calculations, we consider two types of terminations. The zigzag edge of the Pb honeycomb lattice is realized in both of them. The "top" surface also contains a chain of Rh atoms from the kagome lattice. Similarly, the "bottom" surface contains a chain of Rh-Pb atoms from the triangular lattice formed by the Rh kagome net decorated by Pb atoms represented by nonbonded black atoms in Fig. 5(a). Slablike calculations (for ten layers of RhPb) clearly show the existence of surface states, independently of the termination [blue and red lines in Fig. 5(c)]. The phonon dispersion curves, in this case, contain many more branches than the dispersion curves for the bulk [Fig. 3(c)], what is the consequence of projection of all phonon states from the bulk (3D) Brillouin zone onto the 2D Brillouin zone of the surface [see Fig. 5(b)]. It is interesting that, in the case of the surface directly terminated by the zigzag edge of the Pb honeycomb lattice (i.e., top surface), the phonon surface states at the highest frequencies exhibit behavior similar to this observed in electronic surface states at the zigzag edge in
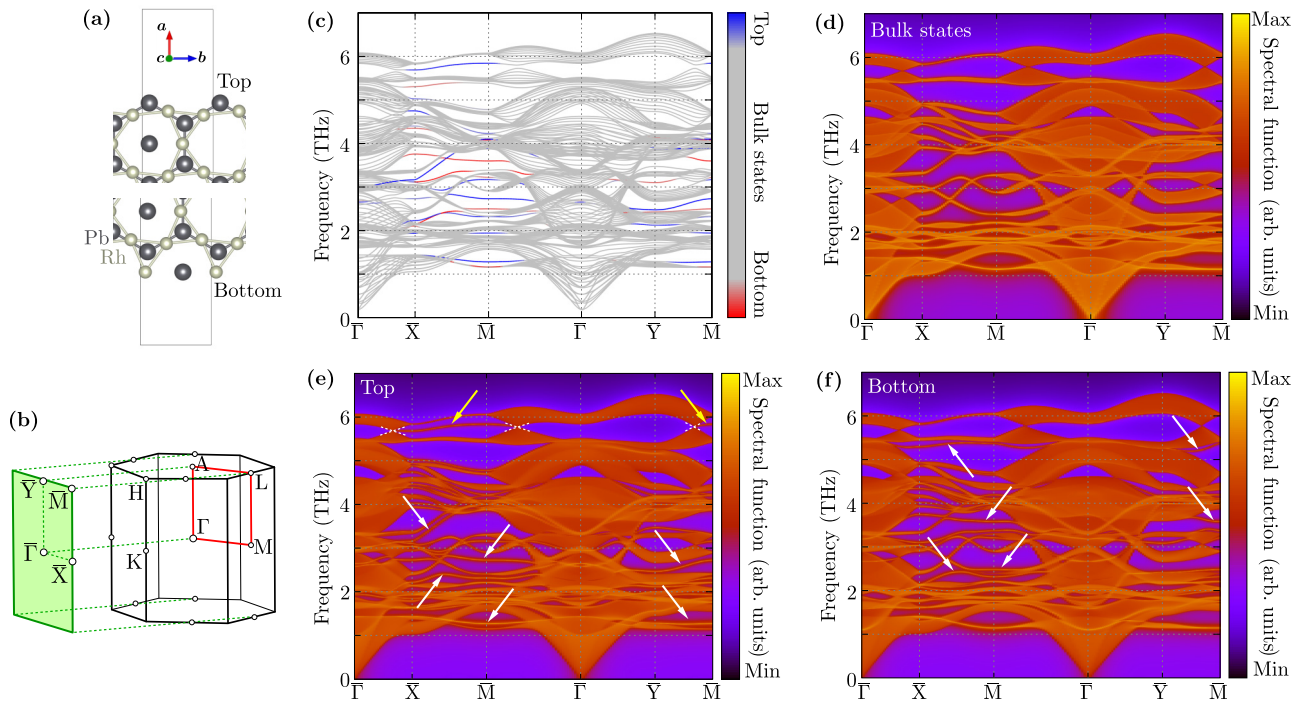

FIG. 5. The phonon surface states realized at the edge of the (100) surfaces of RhPb with $P\bar{6}2m$ symmetry. Surface terminations are presented in panel (a). For simplification, we show only bonding between Rh atoms forming a distorted kagome lattice and Pb atoms forming a honeycomb lattice. The Pb atom in the center of hexagons is placed in the plane of a distorted kagome lattice. (b) Relation between the bulk (3D) and surface (2D) Brillouin zone. Phonon band structure calculated for slablike structure (c), containing ten layers. The colors correspond to the states related to vibrations of the atoms at the top surface (blue), central bulklike part (gray), or bottom surface (red). The panels from (d) to (f) present the spectral function calculated for the central bulklike part, the top surface, and the bottom surface part of the slab, respectively. The arrows in (e) and (f) show the locations of the soft modes of the phonons realized on the top or bottom surfaces, respectively.
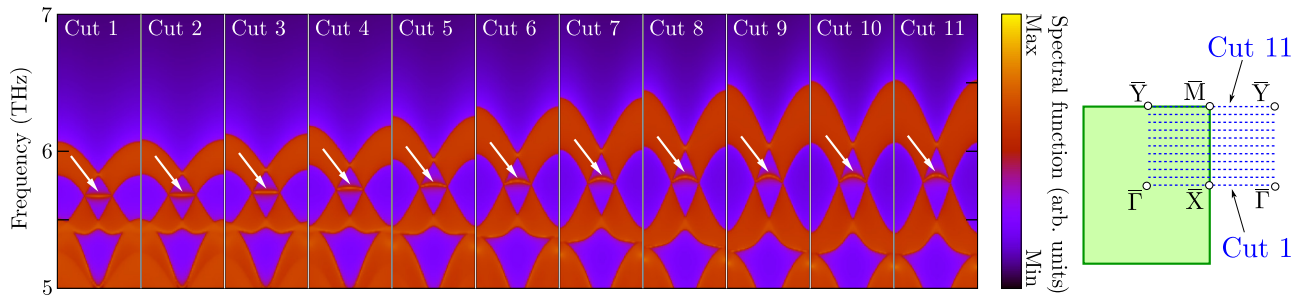
FIG. 6. The surface spectral function for different cuts of the surface (2D) Brillouin zone (right panel), presenting *k*-point dependence of the phonon drumhead surface state (marked with white arrows).

the graphene nanoribbon [102] [see the states with frequencies around 5.75 THz, marked with yellow arrows in Fig. 5(e)].

Direct calculations of the spectral functions for the bulk and surface regions are presented in Figs. 5(d)–5(f). The phonon surface states can be, in a relatively simple way, extracted from the bulk spectra, by comparing the spectral function related to the bulk states [see Fig. 5(d)] with the adequate spectral function for a specific surface [Fig. 5(e) or 5(f)]. Additional states, i.e., surface states, are marked with arrows. Comparing the frequencies of surface states with the bulk phonon DOS [Fig. 3(d)], we see that the surface states in the low (high) frequency range are realized mostly by Pb (Rh) atoms.

Probably, the most interesting properties of the slablike structure can be observed for the highest branches of the spectrum. First, the signature of the bulk Dirac "point" [i.e., Dirac lines from the K-H direction in the 3D bulk Brillouin zone are projected on the 2D surface Brillouin zone, see Fig. 5(b)] can be well recognized in the spectrum [white dashed crosses in Fig. 5(e)]. Between these points, the previously mentioned zigzaglike edge mode is formed.

However, a more precise analysis of this latter state uncovers the realization of the drumhead phononic surface state. Indeed, as one can recognize in Fig. 6, these surface states exists independently of momentum *k*, forming a 2D surface state between the two bulk Dirac lines mentioned earlier. Formation of the drumhead phonon surface state is presented schematically in Fig. 7. Remarkably, the projected bulk phonon surface state creates a graphenelike spectrum, independently of mo-

mentum *k*. Note that the band crossing discussed earlier (red line in Fig. 7) is visible as a Dirac "point" for any value of *k*. Finally, the drumhead surface state is realized between the Dirac nodal lines. It is remarkable that the frequency of the phonon drumhead surface state strongly depends on momentum *k* (see Fig. 6).

IV. SUMMARY

In this paper, we discuss the basic properties of RhPb with the distorted kagome lattice of Rh atoms. Initially presented theoretical calculations [75] predict the realization of the distorted kagome lattice in RhPb. Indeed, our single crystal diffraction results confirm the predicted distortion of the kagome net in RhPb.

We presented a study of the dynamical properties of the bulk RhPb compound. In such a system, the emergence of several flattened phonon bands is possible. However, a more precise analysis shows that phonons in this band have even broader dispersion than for an ideal kagome lattice. This behavior is clearly recognized in the phonon density of states.

The phonon dispersion curves exhibit several interesting features, namely the (bulk) Dirac nodal lines and triple degenerated Dirac points. Such structures have consequences for the observed surface states. The most prominent example is the phonon drumhead surface state, between two (bulk) Dirac nodal lines projected on the surface Brillouin zone. In this context, the RhPb crystal with the distorted kagome lattice is an excellent platform to study the interplay between topological phonon surface states and flat electronic bands.
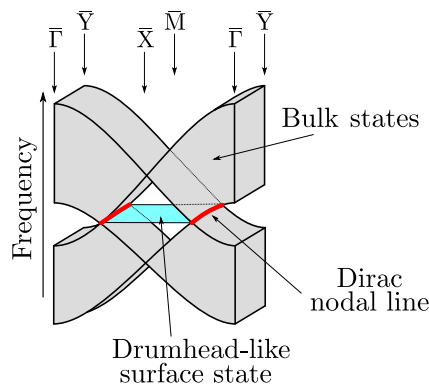
FIG. 7. Schematic representation of the phonon drumhead surface state.

[1] H. Zhang, C.-X. Liu, X.-L. Qi, X. Dai, Z. Fang, and S.-C. Zhang, Topological insulators in Bi_2Se_3, Bi_2Te_3 and Sb_2Te_3 with a single Dirac cone on the surface, Nat. Phys. **5**, 438 (2009).

[2] Y. Xia, D. Qian, D. Hsieh, L. Wray, A. Pal, H. Lin, A. Bansil, D. Grauer, Y. S. Hor, R. J. Cava, and M. Z. Hasan, Observation of a large-gap topological-insulator class with a single Dirac cone on the surface, Nat. Phys. **5**, 398 (2009).

[3] D. Hsieh, Y. Xia, D. Qian, L. Wray, F. Meier, J. H. Dil, J. Osterwalder, L. Patthey, A. V. Fedorov, H. Lin, A. Bansil, D. Grauer, Y. S. Hor, R. J. Cava, and M. Z. Hasan, Observation of time-reversal-protected single-Dirac-cone topological-insulator states in Bi_2Te_3 and Sb_2Te_3, Phys. Rev. Lett. **103**, 146401 (2009).

[4] Z. Alpichshev, J. G. Analytis, J.-H. Chu, I. R. Fisher, Y. L. Chen, Z. X. Shen, A. Fang, and A. Kapitulnik, Stm imaging of electronic waves on the surface of Bi_2Te_3: Topologically protected surface states and hexagonal warping effects, Phys. Rev. Lett. **104**, 016401 (2010).

[5] M. Z. Hasan and C. L. Kane, Colloquium: Topological insulators, Rev. Mod. Phys. **82**, 3045 (2010).

[6] X.-L. Qi and S.-C. Zhang, Topological insulators and superconductors, Rev. Mod. Phys. **83**, 1057 (2011).

[7] N. P. Armitage, E. J. Mele, and A. Vishwanath, Weyl and Dirac semimetals in three-dimensional solids, Rev. Mod. Phys. **90**, 015001 (2018).

[8] L. Lu, J. D. Joannopoulos, and M. Soljačić, Topological photonics, Nat. Photonics **8**, 821 (2014).

[9] Z. Yang, F. Gao, X. Shi, X. Lin, Z. Gao, Y. Chong, and B. Zhang, Topological acoustics, Phys. Rev. Lett. **114**, 114301 (2015).

[10] T. Ozawa, H. M. Price, A. Amo, N. Goldman, M. Hafezi, L. Lu, M. C. Rechtsman, D. Schuster, J. Simon, O. Zilberberg, and I. Carusotto, Topological photonics, Rev. Mod. Phys. **91**, 015006 (2019).

[11] Y. Liu, X. Chen, and Y. Xu, Topological phononics: From fundamental models to real materials, Adv. Funct. Mater. **30**, 1904784 (2020).

[12] P. A. McClarty, Topological magnons: A review, Annu. Rev. Condens. Matter Phys. **13**, 171 (2022).

[13] H. Miao, T. T. Zhang, L. Wang, D. Meyers, A. H. Said, Y. L. Wang, Y. G. Shi, H. M. Weng, Z. Fang, and M. P. M. Dean, Observation of double Weyl phonons in parity-breaking FeSi, Phys. Rev. Lett. **121**, 035302 (2018).

[14] J. Li, Q. Xie, J. Liu, R. Li, M. Liu, L. Wang, D. Li, Y. Li, and X.-Q. Chen, Phononic Weyl nodal straight lines in MgB_2, Phys. Rev. B **101**, 024301 (2020).

[15] J. Li, Q. Xie, S. Ullah, R. Li, H. Ma, D. Li, Y. Li, and X.-Q. Chen, Coexistent three-component and two-component Weyl phonons in TiS, ZrSe, and HfTe, Phys. Rev. B **97**, 054305 (2018).

[16] R. Wang, B. W. Xia, Z. J. Chen, B. B. Zheng, Y. J. Zhao, and H. Xu, Symmetry-protected topological triangular Weyl complex, Phys. Rev. Lett. **124**, 105303 (2020).

[17] Z. J. Chen, R. Wang, B. W. Xia, B. B. Zheng, Y. J. Jin, Y.-J. Zhao, and H. Xu, Three-dimensional Dirac phonons with inversion symmetry, Phys. Rev. Lett. **126**, 185301 (2021).

[18] T. Zhang, Z. Song, A. Alexandradinata, H. Weng, C. Fang, L. Lu, and Z. Fang, Double-Weyl phonons in transition-metal monosilicides, Phys. Rev. Lett. **120**, 016401 (2018).

[19] M. Zhong, Y. Liu, F. Zhou, M. Kuang, T. Yang, X. Wang, and G. Zhang, Coexistence of phononic sixfold, fourfold, and threefold excitations in the ternary antimonide $Zr_3Ni_3Sb_4$, Phys. Rev. B **104**, 085118 (2021).

[20] C. Xie, Y. Liu, Z. Zhang, F. Zhou, T. Yang, M. Kuang, X. Wang, and G. Zhang, Sixfold degenerate nodal-point phonons: Symmetry analysis and materials realization, Phys. Rev. B **104**, 045148 (2021).

[21] P.-F. Liu, J. Li, X.-H. Tu, H. Li, J. Zhang, P. Zhang, Q. Gao, and B.-T. Wang, First-principles prediction of ideal type-II Weyl phonons in wurtzite ZnSe, Phys. Rev. B **103**, 094306 (2021).

[22] J. Liu, W. Hou, E. Wang, S. Zhang, J.-T. Sun, and S. Meng, Ideal type-II Weyl phonons in wurtzite CuI, Phys. Rev. B **100**, 081204(R) (2019).

[23] Q.-B. Liu, Y. Qian, H.-H. Fu, and Z. Wang, Symmetry-enforced Weyl phonons, npj Comput. Mater. **6**, 95 (2020).

[24] Q.-B. Liu, Z. Wang, and H.-H. Fu, Charge-four Weyl phonons, Phys. Rev. B **103**, L161303 (2021).

[25] J. Wang, H. Yuan, Y. Liu, F. Zhou, X. Wang, and G. Zhang, Hourglass Weyl and Dirac nodal line phonons, and drumhead-like and torus phonon surface states in orthorhombic-type KCuS, Phys. Chem. Chem. Phys. **24**, 2752 (2022).

[26] G. Ding, J. Wang, Z.-M. Yu, Z. Zhang, W. Wang, and X. Wang, Single pair of type-III Weyl points half-metals: $BaNiIO_6$ as an example, Phys. Rev. Mater. **7**, 014202 (2023).

[27] Y. Yang, C. Xie, Y. Cui, X. Wang, and W. Wu, Maximally charged single-pair multi-Weyl point phonons in $P23$-type BeH_2, Phys. Rev. B **107**, 054310 (2023).

[28] X. Wang, T. Yang, Z. Cheng, G. Surucu, J. Wang, F. Zhou, Z. Zhang, and G. Zhang, Topological nodal line phonons: Recent advances in materials realization, Appl. Phys. Rev. **9**, 041304 (2022).

[29] G. Liu, Y. Jin, Z. Chen, and H. Xu, Symmetry-enforced straight nodal-line phonons, Phys. Rev. B **104**, 024304 (2021).

[30] C. Xie, H. Yuan, Y. Liu, X. Wang, and G. Zhang, Three-nodal surface phonons in solid-state materials: Theory and material realization, Phys. Rev. B **104**, 134303 (2021).

[31] M. Wang, Y. Wang, Z. Yang, J. Fan, B. Zheng, R. Wang, and X. Wu, Symmetry-enforced nodal cage phonons in Th_2BC_2, Phys. Rev. B **105**, 174309 (2022).

[32] S. Basak, A. Kobiałka, and A. Ptok, Dynamical properties of $T_3Pb_2Ch_2$ (T = Pd, Pt and Ch = S, Se) with transition metal kagome net, Adv. Phys. Res. **2**, 2300025 (2023).

[33] F. Zhou, Z. Zhang, H. Chen, M. Kuang, T. Yang, and X. Wang, Hybrid-type nodal ring phonons and coexistence of higher-order quadratic nodal line phonons in an AgZr alloy, Phys. Rev. B **104**, 174108 (2021).

[34] B. Zheng, B. Xia, R. Wang, Z. Chen, J. Zhao, Y. Zhao, and H. Xu, Ideal type-III nodal-ring phonons, Phys. Rev. B **101**, 100303(R) (2020).

[35] Y. J. Jin, Z. J. Chen, B. W. Xia, Y. J. Zhao, R. Wang, and H. Xu, Ideal intersecting nodal-ring phonons in bcc C_8, Phys. Rev. B **98**, 220103(R) (2018).

[36] B. Zheng, F. Zhan, X. Wu, R. Wang, and J. Fan, Hourglass phonons jointly protected by symmorphic and nonsymmorphic symmetries, Phys. Rev. B **104**, L060301 (2021).

[37] R. Y. Wang, Z. J. Chen, Z. Q. Huang, B. W. Xia, and H. Xu, Classification and materials realization of topologically robust nodal ring phonons, Phys. Rev. Mater. **5**, 084202 (2021).

[38] Z. J. Chen, Z. J. Xie, Y. J. Jin, G. Liu, and H. Xu, Hybrid nodal-ring phonons with hourglass dispersion in $AgAlO_2$, Phys. Rev. Mater. **6**, 034202 (2022).

[39] Y. S. Chen, F. F. Huang, P. Zhou, Z. S. Ma, and L. Z. Sun, Ideal topological phononic nodal chain in K_2O materials class, New J. Phys. **23**, 103043 (2021).

[40] F. Zhou, H. Chen, Z.-M. Yu, Z. Zhang, and X. Wang, Realistic cesium fluogermanate: An ideal platform to realize the topologically nodal-box and nodal-chain phonons, Phys. Rev. B **104**, 214310 (2021).

[41] G. Ding, T. Sun, and X. Wang, Ideal nodal-net, nodal-chain, and nodal-cage phonons in some realistic materials, Phys. Chem. Chem. Phys. **24**, 11175 (2022).

[42] J. Zhu, W. Wu, J. Zhao, H. Chen, L. Zhang, and S. A. Yang, Symmetry-enforced nodal chain phonons, npj Quantum Mater. **7**, 52 (2022).

[43] J. Li, L. Wang, J. Liu, R. Li, Z. Zhang, and X.-Q. Chen, Topological phonons in graphene, Phys. Rev. B **101**, 081403(R) (2020).

[44] J. Wang, H. Yuan, Z.-M. Yu, Z. Zhang, and X. Wang, Coexistence of symmetry-enforced phononic Dirac nodal-line net and three-nodal surfaces phonons in solid-state materials: Theory and materials realization, Phys. Rev. Mater. **5**, 124203 (2021).

[45] Q.-B. Liu, Z.-Q. Wang, and H.-H. Fu, Ideal topological nodal-surface phonons in RbTeAu-family materials, Phys. Rev. B **104**, L041405 (2021).

[46] J. Wang, H. Yuan, M. Kuang, T. Yang, Z.-M. Yu, Z. Zhang, and X. Wang, Coexistence of zero-, one-, and two-dimensional degeneracy in tetragonal SnO_2 phonons, Phys. Rev. B **104**, L041107 (2021).

[47] Q.-B. Liu, H.-H. Fu, and R. Wu, Topological phononic nodal hexahedron net and nodal links in the high-pressure phase of the semiconductor CuCl, Phys. Rev. B **104**, 045409 (2021).

[48] Z. Wang, W. Zhou, A. N. Rudenko, and S. Yuan, Lattice dynamics and topological surface phonon states in cuprous oxide Cu_2O, Phys. Rev. B **103**, 195137 (2021).

[49] Y. Yang, J. Wang, Y. Liu, Y. Cui, G. Ding, and X. Wang, Topological phonons in Cs-Te binary systems, Phys. Rev. B **107**, 024304 (2023).

[50] C. Strohm, G. L. J. A. Rikken, and P. Wyder, Phenomenological evidence for the phonon Hall effect, Phys. Rev. Lett. **95**, 155901 (2005).

[51] L. Sheng, D. N. Sheng, and C. S. Ting, Theory of the phonon Hall effect in paramagnetic dielectrics, Phys. Rev. Lett. **96**, 155901 (2006).

[52] Y. Kagan and L. A. Maksimov, Anomalous Hall effect for the phonon heat conductivity in paramagnetic dielectrics, Phys. Rev. Lett. **100**, 145902 (2008).

[53] L. Zhang, J. Ren, J.-S. Wang, and B. Li, Topological nature of the phonon Hall effect, Phys. Rev. Lett. **105**, 225901 (2010).

[54] T. Qin, J. Zhou, and J. Shi, Berry curvature and the phonon Hall effect, Phys. Rev. B **86**, 104305 (2012).

[55] T. Saito, K. Misaki, H. Ishizuka, and N. Nagaosa, Berry phase of phonons and thermal Hall effect in nonmagnetic insulators, Phys. Rev. Lett. **123**, 255901 (2019).

[56] X. Zhang, Y. Zhang, S. Okamoto, and D. Xiao, Thermal Hall effect induced by magnon-phonon interactions, Phys. Rev. Lett. **123**, 167202 (2019).

[57] L. Zhang and Q. Niu, Chiral phonons at high-symmetry points in monolayer hexagonal lattices, Phys. Rev. Lett. **115**, 115502 (2015).

[58] N. Li, J. Ren, L. Wang, G. Zhang, P. Hänggi, and B. Li, Colloquium: Phononics: Manipulating heat flow with electronic analogs and beyond, Rev. Mod. Phys. **84**, 1045 (2012).

[59] Z. Lin, J.-H. Choi, Q. Zhang, W. Qin, S. Yi, P. Wang, L. Li, Y. Wang, H. Zhang, Z. Sun, L. Wei, S. Zhang, T. Guo, Q. Lu, J.-H. Cho, C. Zeng, and Z. Zhang, Flatbands and emergent ferromagnetic ordering in Fe_3Sn_2 kagome lattices, Phys. Rev. Lett. **121**, 096401 (2018).

[60] J.-X. Yin, S. S. Zhang, G. Chang, Q. Wang, S. S. Tsirkin, Z. Guguchia, B. Lian, H. Zhou, K. Jiang, I. Belopolski, N. Shumiya, D. Multer, M. Litskevich, T. A. Cochran, H. Lin, Z. Wang, T. Neupert, S. Jia, H. Lei, and M. Z. Hasan, Negative flat band magnetism in a spin–orbit-coupled correlated kagome magnet, Nat. Phys. **15**, 443 (2019).

[61] M. Li, Q. Wang, G. Wang, Z. Yuan, W. Song, R. Lou, Z. Liu, Y. Huang, Z. Liu, H. Lei, Z. Yin, and S. Wang, Dirac cone, flat band and saddle point in kagome magnet YMn_6Sn_6, Nat. Commun. **12**, 3129 (2021).

[62] B. C. Sales, J. Yan, W. R. Meier, A. D. Christianson, S. Okamoto, and M. A. McGuire, Electronic, magnetic, and thermodynamic properties of the kagome layer compound FeSn, Phys. Rev. Mater. **3**, 114203 (2019).

[63] W. R. Meier, M.-H. Du, S. Okamoto, N. Mohanta, A. F. May, M. A. McGuire, C. A. Bridges, G. D. Samolyuk, and B. C. Sales, Flat bands in the CoSn-type compounds, Phys. Rev. B **102**, 075148 (2020).

[64] Z. Liu, M. Li, Q. Wang, G. Wang, C. Wen, K. Jiang, X. Lu, S. Yan, Y. Huang, D. Shen, J.-X. Yin, Z. Wang, Z. Yin, H. Lei, and S. Wang, Orbital-selective Dirac fermions and extremely flat bands in frustrated kagome-lattice metal CoSn, Nat. Commun. **11**, 4002 (2020).

[65] H. Huang, L. Zheng, Z. Lin, X. Guo, S. Wang, S. Zhang, C. Zhang, Z. Sun, Z. Wang, H. Weng, L. Li, T. Wu, X. Chen, and C. Zeng, Flat-band-induced anomalous anisotropic charge transport and orbital magnetism in kagome metal CoSn, Phys. Rev. Lett. **128**, 096601 (2022).

[66] M. Kang, S. Fang, L. Ye, H. C. Po, J. Denlinger, C. Jozwiak, A. Bostwick, E. Rotenberg, E. Kaxiras, J. G. Checkelsky, and R. Comin, Topological flat bands in frustrated kagome lattice CoSn, Nat. Commun. **11**, 4004 (2020).

[67] M. Kang, L. Ye, S. Fang, J.-S. You, A. Levitan, M. Han, J. I. Facio, C. Jozwiak, A. Bostwick, E. Rotenberg, M. K. Chan, R. D. McDonald, D. Graf, K. Kaznatcheev, E. Vescovo, D. C. Bell, E. Kaxiras, J. van den Brink, M. Richter, M. Prasad Ghimire *et al.*, Dirac fermions and flat bands in the ideal kagome metal FeSn, Nat. Mater. **19**, 163 (2020).

[68] Z. Lin, C. Wang, P. Wang, S. Yi, L. Li, Q. Zhang, Y. Wang, Z. Wang, H. Huang, Y. Sun, Y. Huang, D. Shen, D. Feng, Z. Sun, J.-H. Cho, C. Zeng, and Z. Zhang, Dirac fermions in antiferromagnetic FeSn kagome lattices with combined space inversion and time-reversal symmetry, Phys. Rev. B **102**, 155103 (2020).

[69] M. Han, H. Inoue, S. Fang, C. John, L. Ye, M. K. Chan, D. Graf, T. Suzuki, M. P. Ghimire, W. J. Cho, E. Kaxiras, and J. G. Checkelsky, Evidence of two-dimensional flat band at the surface of antiferromagnetic kagome metal FeSn, Nat. Commun. **12**, 5345 (2021).

[70] B. C. Sales, W. R. Meier, A. F. May, J. Xing, J.-Q. Yan, S. Gao, Y. H. Liu, M. B. Stone, A. D. Christianson, Q. Zhang, and M. A. McGuire, Tuning the flat bands of the kagome metal CoSn with Fe, In, or Ni doping, Phys. Rev. Mater. **5**, 044202 (2021).

[71] Y. Xie, L. Chen, T. Chen, Q. Wang, Q. Yin, J. R. Stewart, M. B. Stone, L. L. Daemen, E. Feng, H. Cao, H. Lei, Z. Yin, A. H. MacDonald, and P. Dai, Spin excitations in metallic kagome lattice FeSn and CoSn, Commun. Phys. **4**, 240 (2021).

[72] C. Zeng, P. R. C. Kent, M. Varela, M. Eisenbach, G. M. Stocks, M. Torija, J. Shen, and H. H. Weitering, Epitaxial stabilization of ferromagnetism in the nanophase of FeGe, Phys. Rev. Lett. **96**, 127201 (2006).

[73] M. Kakihana, K. Nishimura, D. Aoki, A. Nakamura, M. Nakashima, Y. Amako, T. Takeuchi, T. Kida, T. Tahara, M. Hagiwara, H. Harima, M. Hedo, T. Nakama, and Y. Onuki, Electronic states of antiferromagnet FeSn and Pauli paramagnet CoSn, J. Phys. Soc. Jpn. **88**, 014705 (2019).

[74] D. Khadka, T. R. Thapaliya, J. Wen, R. F. Need, and S. X. Huang, High quality epitaxial thin films and exchange bias of antiferromagnetic dirac semimetal FeSn, Appl. Phys. Lett. **117**, 032403 (2020).

[75] A. Ptok, A. Kobiałka, M. Sternik, J. Łażewski, P. T. Jochym, A. M. Oleś, S. Stankov, and P. Piekarz, Chiral phonons in the honeycomb sublattice of layered CoSn-like compounds, Phys. Rev. B **104**, 054305 (2021).

[76] P. C. Canfield, T. Kong, U. S. Kaluarachchi, and N. H. Jo, Use of frit-disc crucibles for routine and exploratory solution growth of single crystalline samples, Philos. Mag. **96**, 84 (2016).

[77] V. Petříček, M. Dušek, and L. Palatinus, Crystallographic computing system JANA2006: General features, Z. Kristallogr. - Cryst. Mater. **229**, 345 (2014).

[78] P. E. Blöchl, Projector augmented-wave method, Phys. Rev. B **50**, 17953 (1994).

[79] G. Kresse and J. Hafner, *Ab initio* molecular-dynamics simulation of the liquid-metal–amorphous-semiconductor transition in germanium, Phys. Rev. B **49**, 14251 (1994).

[80] G. Kresse and J. Furthmüller, Efficient iterative schemes for *ab initio* total-energy calculations using a plane-wave basis set, Phys. Rev. B **54**, 11169 (1996).

[81] G. Kresse and D. Joubert, From ultrasoft pseudopotentials to the projector augmented-wave method, Phys. Rev. B **59**, 1758 (1999).

[82] J. P. Perdew, K. Burke, and M. Ernzerhof, Generalized gradient approximation made simple, Phys. Rev. Lett. **77**, 3865 (1996).

[83] H. J. Monkhorst and J. D. Pack, Special points for Brillouin-zone integrations, Phys. Rev. B **13**, 5188 (1976).

[84] R. Pott, R. Schefzyk, D. Wohlleben, and A. Junod, Thermal expansion and specific heat of intermediate valent YbCuAl, Z. Phys. B **44**, 17 (1981).

[85] M. S. Kim, Y. Echizen, K. Umeo, S. Kobayashi, M. Sera, P. S. Salamkha, O. L. Sologub, T. Takabatake, X. Chen, T. Tayama, T. Sakakibara, M. H. Jung, and M. B. Maple, Low-temperature anomalies in magnetic, transport, and thermal properties of single-crystal CeRhSn with valence fluctuations, Phys. Rev. B **68**, 054416 (2003).

[86] E. Morosan, S. Bud'ko, P. Canfield, M. Torikachvili, and A. Lacerda, Thermodynamic and transport properties of RAgGe (R = Tb–Lu) single crystals, J. Magn. Magn. Mater. **277**, 298 (2004).

[87] S. F. Matar, J. F. Riecken, B. Chevalier, R. Pöttgen, A. F. Al Alam, and V. Eyert, Electronic and magnetic properties and chemical bonding of CeMSn (M = Rh, Ru) from first principles, Phys. Rev. B **76**, 174434 (2007).

[88] F. R. de Boer, R. A. Elenbaas, and W. C. M. Mattens, Abstract: Mixed valence behaviour in the intermetallic compound YbCuAl, J. Appl. Phys. **49**, 2100 (1978).

[89] Y. Qian, S. Nie, C. Yi, L. Kong, C. Fang, T. Qian, H. Ding, Y. Shi, Z. Wang, H. Weng, and Z. Fang, Topological electronic states in HfRuP family superconductors, npj Comput. Mater. **5**, 121 (2019).

[90] H. Su, T. Shang, F. Du, C. F. Chen, H. Q. Ye, X. Lu, C. Cao, M. Smidman, and H. Q. Yuan, NbReSi: A noncentrosymetric superconductor with large upper critical field, Phys. Rev. Mater. **5**, 114802 (2021).

[91] T. Asaba, V. Ivanov, S. M. Thomas, S. Y. Savrasov, J. D. Thompson, E. D. Bauer, and F. Ronning, Colossal anomalous Nernst effect in a correlated noncentrosymmetric kagome ferromagnet, Sci. Adv. **7**, eabf1467 (2021).

[92] R. Kumar, S.-S. Luo, F. Du, H. Su, J. Zhang, C. Cao, and H. Q. Yuan, Superconductivity in non-centrosymmetric ZrNiAl and HfRhSn-type compounds, J. Phys.: Condens. Matter **34**, 435701 (2022).

[93] See the Supplemental Material at http://link.aps.org/supplemental/10.1103/PhysRevResearch.5.043231 for more details on the crystallographic data, XRD refinements, and additional numerical results. This Supplemental Material contains Ref. [62–66,70,72–74,114–116].

[94] K. Parlinski, Z. Q. Li, and Y. Kawazoe, First-principles determination of the soft mode in cubic ZrO_2, Phys. Rev. Lett. **78**, 4063 (1997).

[95] A. Togo and I. Tanaka, First principles phonon calculations in materials science, Scr. Mater. **108**, 1 (2015).

[96] M. P. L. Sancho, J. M. L. Sancho, J. M. L. Sancho, and J. Rubio, Highly convergent schemes for the calculation of bulk and surface Green functions, J. Phys. F: Met. Phys. **15**, 851 (1985).

[97] Q. S. Wu, S. N. Zhang, H.-F. Song, M. Troyer, and A. A. Soluyanov, WANNIERTOOLS: An open-source software package for novel topological materials, Comput. Phys. Commun. **224**, 405 (2018).

[98] O. Hellman, I. A. Abrikosov, and S. I. Simak, Lattice dynamics of anharmonic solids from first principles, Phys. Rev. B **84**, 180301(R) (2011).

[99] P. T. Jochym and J. Łażewski, High Efficiency Configuration Space Sampling–probing the distribution of available states, SciPost Phys. **10**, 129 (2021).

[100] M. Sinha, H. K. Vivanco, C. Wan, M. A. Siegler, V. J. Stewart, E. A. Pogue, L. A. Pressley, T. Berry, Z. Wang, I. Johnson, M. Chen, T. T. Tran, W. A. Phelan, and T. M. McQueen, Twisting of 2D kagome sheets in layered intermetallics, ACS Cent. Sci. **7**, 1381 (2021).

[101] J.-X. Yin, N. Shumiya, S. Mardanya, Q. Wang, S. S. Zhang, H.-J. Tien, D. Multer, Y. Jiang, G. Cheng, N. Yao, S. Wu, D. Wu, L. Deng, Z. Ye, R. He, G. Chang, Z. Liu, K. Jiang, Z. Wang, T. Neupert *et al.*, Fermion–boson many-body interplay in a frustrated kagome paramagnet, Nat. Commun. **11**, 4003 (2020).

[102] L. Brey and H. A. Fertig, Electronic states of graphene nanoribbons studied with the Dirac equation, Phys. Rev. B **73**, 235411 (2006).

[103] K. Wakabayashi, Y. Takane, and M. Sigrist, Perfectly conducting channel and universality crossover in disordered graphene nanoribbons, Phys. Rev. Lett. **99**, 036601 (2007).

[104] W. Yao, S. A. Yang, and Q. Niu, Edge states in graphene: From gapped flat-band to gapless chiral modes, Phys. Rev. Lett. **102**, 096801 (2009).

[105] B.-J. Yang and N. Nagaosa, Emergent topological phenomena in thin films of pyrochlore iridates, Phys. Rev. Lett. **112**, 246402 (2014).

[106] Z. Li, J. Zhuang, L. Wang, H. Feng, Q. Gao, X. Xu, W. Hao, X. Wang, C. Zhang, K. Wu, S. X. Dou, L. Chen, Z. Hu, and Y. Du, Realization of flat band with possible nontrivial topology in electronic kagome lattice, Sci. Adv. **4**, eaau4511 (2018).

[107] A. Mook, J. Henk, and I. Mertig, Edge states in topological magnon insulators, Phys. Rev. B **90**, 024412 (2014).

[108] D. Malz, J. Knolle, and A. Nunnenkamp, Topological magnon amplification, Nat. Commun. **10**, 3937 (2019).

[109] H. Zhong, R. Wang, F. Ye, J. Zhang, L. Zhang, Y. Zhang, M. R. Belić, and Y. Zhang, Topological insulator properties of photonic kagome helical waveguide arrays, Results Phys. **12**, 996 (2019).

[110] X. Xi, J. Ma, S. Wan, C.-H. Dong, and X. Sun, Observation of chiral edge states in gapped nanomechanical graphene, Sci. Adv. **7**, eabe1398 (2021).

[111] S. Basak and A. Ptok, Theoretical study of dynamical and electronic properties of noncentrosymmetric superconductor NbReSi, Materials **16**, 78 (2023).

[112] K. Momma and F. Izumi, VESTA3 for three-dimensional visualization of crystal, volumetric and morphology data, J. Appl. Crystallogr. **44**, 1272 (2011).

[113] A. Kokalj, Xcrysden–a new program for displaying crystalline structures and electron densities, J. Mol. Graphics Modell. **17**, 176 (1999).

[114] M. Jovanovic and L. M. Schoop, Simple chemical rules for predicting band structures of kagome materials, J. Am. Chem. Soc. **144**, 10978 (2022).

[115] F. Herman, C. D. Kuglin, K. F. Cuff, and R. L. Kortum, Relativistic corrections to the band structure of tetrahedrally bonded semiconductors, Phys. Rev. Lett. **11**, 541 (1963).

[116] K. V. Shanavas, Z. S. Popović, and S. Satpathy, Theoretical model for Rashba spin-orbit interaction in d electrons, Phys. Rev. B **90**, 165108 (2014).

[117] https://www.humboldt-foundation.de/web/humboldt-preis.html.